Monthly Notices
of the
ROYAL ASTRONOMICAL SOCIETY

MNRAS **462,** 994–1001 (2016)
Advance Access publication 2016 July 14

doi:10.1093/mnras/stw1670

Bursty star formation feedback and cooling outflows

Teresita Suarez,[1⋆] Andrew Pontzen,[1⋆] Hiranya V. Peiris,[1] Adrianne Slyz[2] and Julien Devriendt[2]

[1]*Department of Physics and Astronomy, University College London, London WC1E 6BT, UK*
[2]*Oxford Astrophysics, Denys Wilkinson Building, Keble Road, Oxford OX1 3RH, UK*

Accepted 2016 July 8. Received 2016 July 1; in original form 2016 March 14

ABSTRACT

We study how outflows of gas launched from a central galaxy undergoing repeated starbursts propagate through the circum-galactic medium (CGM), using the simulation code RAMSES. We assume that the outflow from the disc can be modelled as a rapidly moving bubble of hot gas at ∼1 kpc above disc, then ask what happens as it moves out further into the halo around the galaxy on ∼100 kpc scales. To do this, we run 60 two-dimensional simulations scanning over parameters of the outflow. Each of these is repeated with and without radiative cooling, assuming a primordial gas composition to give a lower bound on the importance of cooling. In a large fraction of radiative-cooling cases we are able to form rapidly outflowing cool gas from *in situ* cooling of the flow. We show that the amount of cool gas formed depends strongly on the 'burstiness' of energy injection; sharper, stronger bursts typically lead to a larger fraction of cool gas forming in the outflow. The abundance ratio of ions in the CGM may therefore change in response to the detailed historical pattern of star formation. For instance, outflows generated by star formation with short, intense bursts contain up to 60 per cent of their gas mass at temperatures $<5 \times 10^4$ K; for near-continuous star formation, the figure is $\lesssim$5 per cent. Further study of cosmological simulations, and of idealized simulations with e.g. metal-cooling, magnetic fields and/or thermal conduction, will help to understand the precise signature of bursty outflows on observed ion abundances.

Key words: hydrodynamics – galaxies: haloes – intergalactic medium.

1 INTRODUCTION

Star-forming galaxies are surrounded by gas (known as the circum-galactic medium, CGM) with a comparable total mass to their stellar mass (Werk et al. 2014). This gas is enriched by metals that were almost certainly ejected from the galaxy; outflows, carrying a mass comparable to the mass of star-forming regions, are ubiquitously observed in star-forming galaxies in the local Universe (Strickland et al. 2004; Erb 2015), at intermediate redshifts $z \sim 0.5$ (Rubin et al. 2010; Nielsen, Churchill & Kacprzak 2013; Bordoloi et al. 2014) and at high redshifts of $z \sim 6$ (Ajiki et al. 2002; Martin 2005). The interrelationship between inflow and outflow is critical to the behaviour of galaxies as a whole, as it reshapes quantities such as the stellar mass function (Dekel & Silk 1986; Oppenheimer et al. 2010) and mass–metallicity relation (Finlator & Davé 2008). Baryon cycling through the CGM likely also plays a role in controlling the distribution of dark matter (Pontzen & Governato 2014; Pontzen et al. 2015).

The mechanism behind outflows is uncertain and may relate to some combination of supernova (SN) feedback (Governato et al. 2010), winds of high-mass stars (Martin 1999; Dalla Vecchia & Schaye 2008) and active galactic nuclei (AGN; Nesvadba et al. 2008). Dwarf galaxies are of particular interest since their small black hole masses makes AGN feedback ineffective, so that the outflows are almost certainly linked directly to star formation feedback. Additionally, the higher gas-to-stellar-mass fraction combined with the shallow gravitational potential allow outflows to easily release material to the CGM (Peeples et al. 2014). Observations in this low-mass regime have shown evidence of C IV absorption in the CGM out to 100 kpc. Therefore, these galaxies are useful case studies of the connection between the CGM and the host galaxy.

Galactic outflows seem to possess a multiphase nature, spanning several orders of magnitude in temperature (Werk et al. 2014). There is a particular puzzle over how cold gas material could survive in galactic outflows if they are entrained in a hot flow (e.g. Veilleux, Cecil & Bland-Hawthorn 2005; Scannapieco & Brüggen 2015; Zhang et al. 2015). Perhaps, this implies that cold gas can be directly accelerated using radiation pressure (Murray, Quataert & Thompson 2005; Hopkins, Quataert & Murray 2012). The lifetime of cold clouds is, however, dependent on physical assumptions and

⋆ E-mail: teresita.noguez.13@ucl.ac.uk (TS); a.pontzen@ucl.ac.uk (AP)

simulation methods, meaning that robust conclusions are difficult to draw. Another scenario is that the cooler phases of the outflow are actually formed *in situ* by radiative cooling (e.g. Efstathiou 2000; Martin et al. 2015); recently, detailed analytic discussions in support of this possibility have been given by Thompson et al. (2016) and Bustard, Zweibel & D'Onghia (2016).

In this paper, we study the formation of cool gas in outflows in a different way. Instead of developing analytic solutions to the outflow problem, we inject hot gas into a idealized galaxy halo with a fixed potential. The numerical setup is similar to that of Mac Low & Ferrara (1999) but introduces a simple prescription to deliver the outflow in discrete bursts. While our setup is highly simplified, we use it to argue that the balance between hot and cooler gas will be affected by the duty cycle of star formation. Such a link introduces a new dimension to the relationship between outflows and the evolution of a galaxy, raising the possibility that the relative abundance of different observed ions reflects information about the detailed star formation history. Since it is specifically bursty star formation that can have a profound impact on dark matter and stellar dynamics (Pontzen & Governato 2014), cross-checking typical star formation patterns in the observed Universe would be a valuable additional benefit to studies of the CGM. The simulations are two-dimensional, allowing us to run a much larger parameter study than would be possible in a three-dimensional study.

This paper is organized as follows. In Section 2, we explain the initial and boundary conditions to simulate outflows in galaxies using RAMSES (Teyssier 2002). We discuss the results in Section 3. Finally, we summarize in Section 4.

2 HYDRODYNAMICAL SIMULATIONS

Our aim is to run a series of simulations that track how gas ejected from the disc of a galaxy interacts with halo gas out to the virial radius using RAMSES, a tree-based adaptive mesh refinement hydrodynamical code. We set up an idealized equilibrium halo, then inject hot outflows at the bottom of the computational box according to different models. To allow us to probe a large number of different scenarios, we use two-dimensional simulations.

In Fig. 1, we show a schematic representation of the CGM box in RAMSES. The galaxy is notionally positioned $d_{\rm gal} = 1$ kpc below the bottom of the box and it is not part of our simulations. Instead, we assume hot gas from SNe and other stellar feedback processes is expelled by the galaxy according to parameters that are described in Section 2.2. The lateral and top sides of the box are chosen to satisfy outflow conditions, meaning that RAMSES sets gradients across them to zero. This way, we allow gas to flow outside the box into the intergalactic medium (IGM).

For simplicity of setting up an equilibrium halo (which we discuss further in Section 2.1), we assume a plane-parallel configuration so that the gravity is everywhere in a downwards direction. We assume a fixed gravitational field g corresponding to that of a Navarro–Frenk–White (NFW) dark matter halo, but directed along the $\hat{\boldsymbol{y}}$-direction. This gives us a force law

$$g = -\frac{4\pi G\rho_0 r_{\rm s}^3}{y^2}\left[\log\left(\frac{y+r_{\rm s}}{r_{\rm s}}\right) - \frac{y}{y+r_{\rm s}}\right], \quad (1)$$

where ρ_0 and $r_{\rm s}$ are the scale density and radius of the NFW profile, respectively. It will help to define the virial radius r_{200} which is the radius containing a mean density 200 times that of the cosmological critical value. Our focus is on dwarf galaxies for the reasons outlined in the introduction; accordingly, we use a halo with virial velocity $v_{200} = 50\,{\rm km\,s^{-1}}$, giving a virial radius $r_{200} \simeq 140(1+z)^{-3/2}$ kpc and virial mass $M_{200} \simeq 8 \times 10^{10}\,(1+z)^{-3/2}\,{\rm M}_\odot$. We adopt the scale radius $r_{\rm s} = 5$ kpc from the fit given by Macciò et al. (2007).

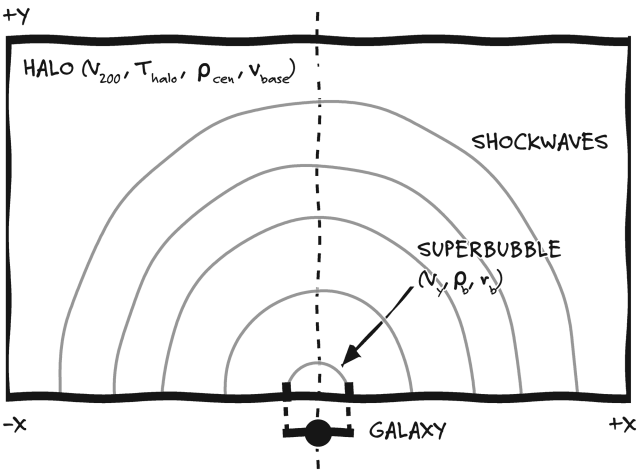

Figure 1. A schematic representation of the two-dimensional setup of our simulation. In our model, gas is assumed to flow into the box along the lower edge, i.e. at $y = 0$, and flow out of the box along each of the remaining three edges. We model half the halo with a radius of approximately 100 kpc. The superbubble is referred to a starburst-type galaxy that is not part of the simulation. The physical properties of the gas expelled by the galaxy determine the boundary conditions in our simulations such as $r_{\rm b} \sim 4$ kpc, $v_{\rm y} \sim 400\,{\rm km\,s^{-1}}$, and a density $\rho_{\rm b} \sim 0.05\rho_{\rm cen}$, as well as the ghost regions that delimit the box. The physical properties of the halo such as v_{200}, $T_{\rm halo}$, $\rho_{\rm cen}$ and $v_{\rm base}$ determine the initial conditions.

The mesh in RAMSES is defined on a recursively refined spatial tree. We set the maximum level of refinement to 10, which means that the regular Cartesian grid is continuously refined in the course of the simulation by a factor of up to $2^{10} = 1024$; our box size of 80 kpc therefore allows for a maximum resolution of 80 pc. We ran a convergence test with higher resolution on one case, reaching 40 pc by increasing the maximum refinement to 11, finding that the results that we describe below did not change. The refinement strategy opens a new cell if the discontinuity in density or pressure is above 5 per cent; for time stepping, we adopted a Courant number of 0.6.

2.1 Initial conditions: equilibrium inflow

We modified the RAMSES code in order to set up equilibrium, inflowing (or hydrostatic) gas in our fixed potential to represent the halo and to inject hot gas in the bottom. Here we discuss the initial equilibrium, then discuss the injection method in Section 2.2.

We ran simulations both with and without cooling. While a hydrostatic solution is an attractive initial stable state in terms of its simplicity, there are no such solutions when cooling is enabled. Therefore, we always consider inflowing gas. The first fluid motion equation enforces mass conservation so that for any region, the rate of change of its mass is the net flow of mass into it:

$$\frac{\partial\rho}{\partial t} + \rho\frac{\partial u}{\partial y} + u\frac{\partial\rho}{\partial y} = 0, \quad (2)$$

where $\rho(y)$ is the density, $u(y)$ is the velocity in the y-direction, and t denotes time. The momentum-conservation equation ensures the rate of change of momentum is balanced by momentum flow and net force:

$$\rho\frac{\partial u}{\partial t} + \rho u\frac{\partial u}{\partial y} = -\frac{\partial p}{\partial y} - \rho g, \quad (3)$$

where p is the pressure. Finally, we have the energy conservation equation:

$$\frac{\partial E}{\partial t} + \frac{\partial}{\partial y}[(E+p)u] = -\rho\,\dot{Q}_{\rm cool} + \rho\frac{\partial \Phi}{\partial t}, \tag{4}$$

where $E = \rho(\epsilon + u^2/2 + \Phi)$ refers to the energy per unit volume, ϵ is the internal energy per unit mass, Φ is the potential implied by equation (1), and the cooling function is defined by $\dot{Q}_{\rm cool}(\rho, T)$ per unit mass. We substitute for the internal energy

$$\epsilon = \frac{3kT}{2\mu m_{\rm p}}, \tag{5}$$

where k is the Boltzmann constant, $m_{\rm p}$ is the proton mass, and μ is the mean molecular weight of the gas constituents. We assume a primordial gas for our background solution, and furthermore that μ is constant (i.e. the ionization is fixed), and check that this assumption holds by ensuring the resulting initial conditions are stable over many sound-crossing times.

To obtain the equilibrium halo solution, we then set all partial derivatives with respect to t to be zero. Overall, once simplified using equation (2), the energy equation, equation (4), becomes

$$u\frac{\partial u}{\partial y} + \frac{5k}{2\mu m_{\rm p}}\frac{\partial T}{\partial y} = g - \frac{\dot{Q}_{\rm cool}}{u}. \tag{6}$$

Finally, we solve the three equations above for $\partial u/\partial y$, $\partial \rho/\partial y$ and $\partial T/\partial y$:

$$\frac{\partial u}{\partial y} = \frac{-2\dot{Q}_{\rm cool} + 3\,gu}{-5\tilde{R}T + 3u^2}, \tag{7}$$

$$\frac{\partial \rho}{\partial y} = -\frac{\rho}{u}\frac{\partial u}{\partial y} \qquad \text{and} \tag{8}$$

$$\frac{\partial T}{\partial y} = 2\,\frac{(\dot{Q}_{\rm cool}/u)\tilde{R}T + g\tilde{R}T - \dot{Q}_{\rm cool}u}{k(-5\tilde{R}T + 3u^2)}, \tag{9}$$

where $\tilde{R} = k/\mu m_{\rm p}$. Note that the denominator can cross zero, corresponding to a shock in the inflow solution, but by studying only low-mass galaxies, we do not suffer from this potential problem (Rees & Ostriker 1977). We used equations (7)–(9) in conjunction with a numerical Runge–Kutta integrator to obtain initial conditions.

We required two solutions: one for the adiabatic case when we set $\dot{Q}_{\rm cool} = 0$ and the other for cooling simulations. In the latter case, we obtain $\dot{Q}_{\rm cool}$ from the RAMSES cooling function assuming primordial gas composition and a UV background fixed to the Haardt & Madau (2012) normalization at $z = 2$. At lower redshifts, metal enrichment and a reduced UV background would lead to faster cooling. Therefore, our results will give a lower bracket for the amounts of cool gas that can be generated in outflows.

We have freedom in imposing conditions $\rho(0)$, $u(0)$ and $T(0)$ (i.e. the density, velocity and temperature 1 kpc above the notional galaxy). Our primary criteria for choosing these was to obtain a CGM with (i) a density of around 10^4 $M_\odot$ kpc^{-3} at $y = 0$ reducing to around 10^3 $M_\odot$ kpc^{-3} at the virial radius; (ii) an overall temperature of around 3×10^5 K; (iii) a small inflow velocity $\lesssim$5 km s^{-1} at the base of the box. These choices were motivated by the inflowing component of the CGM of the cosmological zoom simulation DG1 from Pontzen & Governato (2012).

Achieving these goals requires a different solution for the adiabatic and cooling cases. Fig. 2 shows the two solutions as, respectively, a dashed and solid line, illustrating (from top to bottom) the temperature, density and velocity. We tuned by hand to find solutions as similar as possible between the two cases. The biggest difference between cooling and adiabatic cases is that, when cooling is enabled, the temperature drops rapidly as inflowing gas nears the bottom of the box. This also implies that the density increases rapidly in the same region.

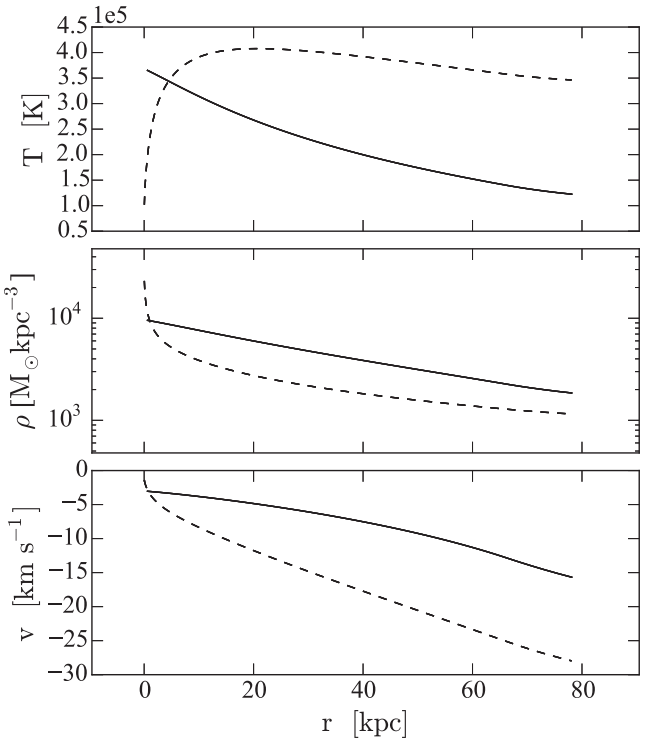

Figure 2. Equilibrium inflow conditions that we adopted as a function of height. These are obtained by solving equations (7)–(9). The solid line represents the adopted solution for adiabatic runs (i.e. $\dot{Q}_{\rm cool} = 0$). The solution when cooling is activated is represented by the dashed lines.

Overall, we found two solutions with similar overall parameters for the undisturbed CGM, and were able to verify that these were indeed stable by running them for several Gyr in RAMSES.

2.2 Outflow characterization

In the previous section, we described the physical properties of inflowing gas, setting our initial conditions. We now consider the boundary conditions which include the properties of the 'superbubble' emerging from the galaxy, assuming a single phase outflow uniformly distributed across a radius of $r_{\rm b}$. The properties of the new hot material are characterized by the radius, the density of the new gas ($\rho_{\rm b}$) and its upwards velocity (v_y). The temperature of the superbubble is set for pressure equilibrium so that $p_{\rm b} = p_{\rm base}$, otherwise pressure would cause it to rapidly expand. Since $p \propto \rho T$, the temperature and density of the bubble and inflow are interrelated by $T_{\rm bub}/T_{\rm base} = \rho_{\rm base}/\rho_{\rm b}$. We assume that the outflow is dominated by a hot phase with $T_{\rm bub} \gg T_{\rm base}$, ignoring any colder material that may have been transported from the disc. While it may be possible to accelerate cold clouds, preventing their disruption over a few scalelengths is challenging (Scannapieco & Brüggen 2015) and consequently on large scales, *in situ* cooling is likely to be a strongly dominant source of cool outflows (Thompson et al. 2016).

The main aim of the current paper is to investigate how *in situ* cooling changes as the nature of the star formation cycle in the

galaxy is altered. To allow us to parametrize this and investigate systematic changes, we define a cycle length $t_{\rm cyc}$ and duty cycle $f_{\rm cyc}$. The cycle length is the overall time periodicity of the galactic star formation. The duration of the whole simulation is always set for at least five times the cycle length, which means that multiple bubbles are injected. The duty cycle is the fraction of time that the bubble actually spends pumping gas into the halo, so that $f_{\rm cyc} = 0$ implies no bubble is created, whereas $f_{\rm cyc} = 1$ means that the galaxy expels gas at all times. Our cycle is deterministic; in this work, we have not investigated the modifications that randomness within the duty cycle could introduce.

The two parameters $t_{\rm cyc}$ and $f_{\rm cyc}$ are of particular interest because they characterize a 'burstiness' for the star formation; bursts of star formation are also important to determine whether dark matter cusp/core transformations are generated by the outflows (Pontzen & Governato 2014). In galaxy formation simulations, the burstiness of star formation is strongly affected by the feedback prescription (e.g. Le Bret et al. 2015; Oñorbe et al. 2015). We allow $t_{\rm cyc}$ and $f_{\rm cyc}$ to vary independently in, respectively, eight and five steps, making a grid of 40 models. The values vary between 100 and 3000 Myr for $t_{\rm cyc}$ and between 0.033 and 1.0 for $f_{\rm cyc}$.

When outflows are being generated, the amount of gas produced per unit time ($\dot{M}_{\rm on}$) is determined by the velocity, the density and the radius of the bubble as

$$\dot{M}_{\rm on} = 2(\pi r_{\rm b}^2) v_y \rho_{\rm b}, \tag{10}$$

where the factor of 2 arises from assuming outflows to occur in both directions from the disc. In our scheme, the overall outflow rate is also dependent on the time that the galaxy is expelling gas, i.e. the averaged outflow rate is set by $\dot{M}_{\rm av} = \dot{M}_{\rm on} f_{\rm cyc}$. The total amount of gas expelled by such galaxies is very uncertain, and, because it is too diffuse, halo gas is extremely difficult to observe directly (Werk et al. 2014). We enforce in all our simulations that $\dot{M}_{\rm av} \simeq 0.01\,{\rm M}_\odot\,{\rm yr}^{-1}$, motivated by mass-loading factors of order unity, coupled to low-average star formation rates expected for systems of this size (Governato et al. 2010; Christensen et al. 2016). Consequently, $\dot{M}_{\rm on}$ must vary as $f_{\rm cyc}$ changes in our simulations. Specifically, there is the following relationship between our parameters:

$$\frac{\dot{M}_{\rm av}}{0.01\,{\rm M}_\odot\,{\rm yr}^{-1}} = \frac{v_y}{400\,{\rm km\,s}^{-1}} \frac{\rho_{\rm b}}{490\,{\rm M}_\odot\,{\rm kpc}^{-3}} \left(\frac{r_{\rm b}}{4\,{\rm kpc}}\right)^2 f_{\rm cyc}. \tag{11}$$

The default parameters here have again been motivated by a study of DG1. We fix the left-hand-side of this relationship but vary $f_{\rm cyc}$, so are forced to change other parameters of the outflow. While there is no unique prescription for this, we chose to fix v_y (so that the outflows are always strongly supersonic) and $r_{\rm b}$ (because this is limited by the size of the disc), allowing $\rho_{\rm b}$ to change $\propto f_{\rm cyc}^{-1}$ in compensation. In our most extreme case of $f_{\rm cyc} = 0.033$, $\rho_{\rm b} \simeq 1.7 \times 10^4\,{\rm M}_\odot\,{\rm kpc}^{-3} \simeq 7 \times 10^{-4}\,{\rm amu\,cm}^3 \simeq 0.7\rho_{\rm base}$. Note that there is no dependence on $t_{\rm cyc}$, so that our models at fixed $f_{\rm cyc}$ have identical outflow parameters.

Because the velocities are quite substantial, most of the energy of our bubbles is tied up in kinetic form (even though in the disc, where pressures are substantially higher, the energy may have been thermal). The total energy available from SN explosions is dependent on the stellar initial mass function, but is approximately 10^{49} erg per solar mass of stars formed. The velocity of a wind driven by this energy source is

$$v_y \simeq \sqrt{\epsilon/0.1\eta} \times 300\,{\rm km\,s}^{-1}, \tag{12}$$

Table 1. Parameters describing initial and boundary conditions for the models, motivated by matching on to existing ab initio galaxy simulations as explained in the text. The steady-state background inflow solutions are determined by the first three parameters and vary between cooling and non-cooling simulations to better match the mean properties of the haloes. Instantaneous properties of the 'bubble' emerging into the bottom of our box are given by the next three parameters. The final two parameters, $f_{\rm cyc}$ and $t_{\rm cyc}$, describe the cycle of outflow activity. To keep the time-averaged outflow rate $\dot{M}_{\rm av}$ the same between simulations, $\rho_{\rm b}$ is allowed to depend on $f_{\rm cyc}$.

Quantity	Values (cooling)	Values (adiabatic)
$T_{\rm base}$	6×10^4 K	3×10^5 K
$\rho_{\rm base}$	10^{-3} amu cm^{-3} $= 2.5\times 10^4$ M$_\odot$ kpc^{-3}	3×10^{-4} amu cm^{-3} $= 7.4\times 10^3$ M$_\odot$ kpc^{-3}
$v_{\rm base}$	2 km s^{-1}	3 km s^{-1}
$r_{\rm b}$	4 kpc	
$\rho_{\rm b}/\rho_{\rm base}$	$0.02/f_{\rm cyc}$ (maintaining $\dot{M}_{\rm av}$)	
v_y	400 km s^{-1}	
$t_{\rm cyc}$	Vary between 100 and 3000 Myr	
$f_{\rm cyc}$	Vary between 0.033 and 1	

where ϵ is the fraction of 10^{49} erg M$_\odot^{-1}$ that actually couples and η is the mass-loading factor of the wind, i.e. $\eta = \dot{M}_{\rm av}/\dot{M}_\star$, where $\dot{M}_\star$ is the star formation rate. Our chosen parameters are consistent in the sense that recent simulations find order-unity mass-loading η, while adopting values of ϵ that are at least 0.1 and often considerably more (Governato et al. 2010; Hopkins et al. 2014). As we will see in the next section, the typical outflow velocities that would be observed along a random sightline through the halo is normally considerably less than the imposed outflow velocity at the bottom of our box, since the energy is rapidly dispersed in the halo.

We summarize the values of both the initial and bubble conditions in Table 1.

3 RESULTS

As we explained in Section 2 and Table 1 above, our exploration is based on a 8 × 5 grid of parameters $t_{\rm cyc}$ and $f_{\rm cyc}$. Note that when $f_{\rm cyc} = 1$, the $t_{\rm cyc}$ parameter has no effect, so we can eliminate seven of the simulations from the grid. We allow each simulation to run for >12 Gyr so that the behaviour is not sensitive to the precise details of the initial conditions, even in the cases with a long $t_{\rm cyc}$.

We made an initial visual inspection to classify the morphology of the outflow, finding that the duty cycle causes the adiabatic runs to fall into distinct regimes. Some example outputs are illustrated in Fig. 3. The top row shows the simulation with $f_{\rm cyc} = 0.033$, $t_{\rm cyc} = 0.5$ Gyr, whereas the lower row is generated from simulations with $f_{\rm cyc} = 0.75$, $t_{\rm cyc} = 0.5$ Gyr. The simulations are pictured at $t = 5.9$ Gyr, after a repeatable cycle has been established.

In each row, the two left-hand panels show log gas density ρ over the range $10\,{\rm M}_\odot\,{\rm kpc}^{-3} \le \rho \le 10^6\,{\rm M}_\odot\,{\rm kpc}^{-3}$ for the non-cooling and the cooling simulation. The final panel shows the temperature in the cooling case, scaled within the range $10^4\,{\rm K} \le T \le 10^7\,{\rm K}$. Arrows indicate the velocity vectors of gas cells in the halo.

At any given time, the morphology of all our simulations roughly falls into one of three categories.

(i) Shock-dominated, where the morphology of the density and temperature maps is dominated by roughly spherical, discontinuous fluid flows (see e.g. top-left panel of Fig. 3). These predominantly occur when $t_{\rm cyc}$ is long and/or $f_{\rm cyc}$ is small; the halo is able to

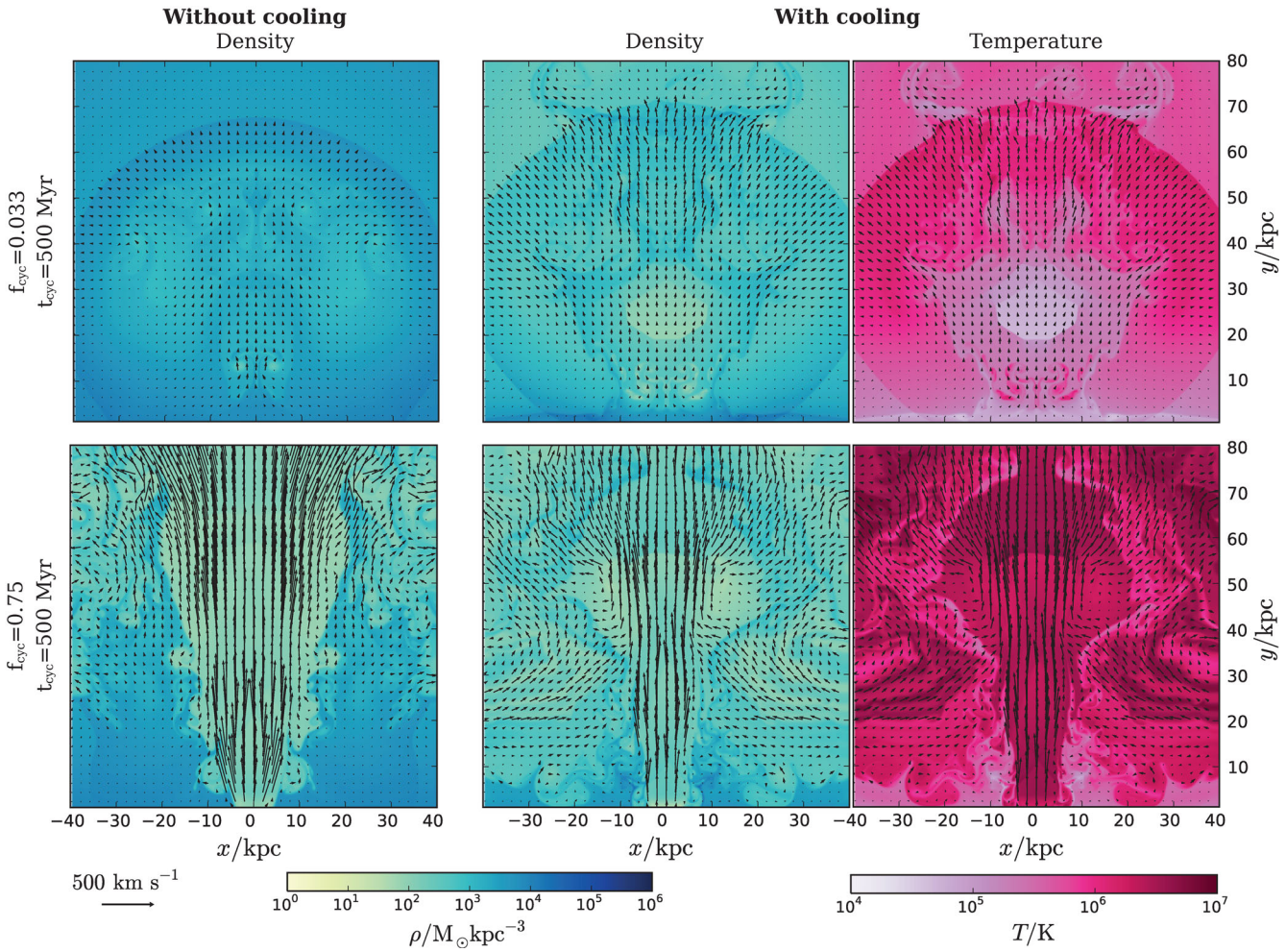

Figure 3. Example renderings of our simulations after several Gyr. The top row shows a short duty cycle example with $t_{cyc} = 500$ Myr and $f_{cyc} = 0.033$. The bottom row shows a long duty cycle example with $t_{cyc} = 500$ Myr and $f_{cyc} = 0.75$. From left to right the panels show the density in the non-cooling (adiabatic) simulations, the density with cooling enabled, and the temperature with cooling enabled.

settle down between each 'burst' of wind injection which therefore triggers a significant shock wave.

(ii) Chimney-dominated, with a morphology which is more dominated by a classic chimney- or funnel-shaped, relatively smooth flow of gas (see e.g. bottom-left panel of Fig. 3). These can only be seen in our simulations with large f_{cyc} or t_{cyc}, which allows the prolonged outflows to 'punch through' the inflowing material. The halo material outside the main outflow often ends up being very turbulent in these cases.

(iii) Intermediate outflows have morphologies that share characteristics of the two types.

A single simulation can switch between the three phases above during its evolution. However, typically shocks can only dominate for a limited time after the outflow switches on, after which it sweeps out of the halo into the IGM beyond our box. When f_{cyc} is small (such as in the top row of Fig. 3), the entire outflow consists of a series of outgoing shocks and a chimney never establishes itself. Conversely, when f_{cyc} is large, the outflow normally looks like a classic chimney pattern. Cases with intermediate f_{cyc} values and large t_{cyc} can switch between the two morphologies depending on the time of observation.

As a rough illustration of this point, Fig. 4 shows our classification for the dominant morphology of each simulation. Shock-dominated outflows are represented with red diamonds and chimney-dominated cases with blue stars. Green crosses indicate the intermediate type where no clear classification can be decided on because it is strongly time-dependent.

Comparing the upper-left panel and upper-mid panels of Fig. 3, we can see that once cooling is enabled, the shocks have a different structure. The shell of dense material caused by the initial shock is able to cool efficiently and so the highest densities are formed behind the shock-front. In the illustrated snapshot, the shock from the most recent episode has reached around 70 kpc above the galaxy; above this are the remains of the previous shock sweeping through the halo. Behind the shock front, the dense gas reaches a regime where its radiative cooling time is short. The typical outflow speeds in the illustrated halo are $\sim$70 km s^{-1}; because the bursts of high-velocity outflows are so short, the initial energy is rapidly spread across a greater mass of gas, making for high-mass loadings but lower velocities in the halo.

Conversely, high-velocity cold gas is typically not generated in large quantities in simulations with a large f_{cyc}, where the chimney is the dominant morphology. The lower panels of Fig. 3 show how

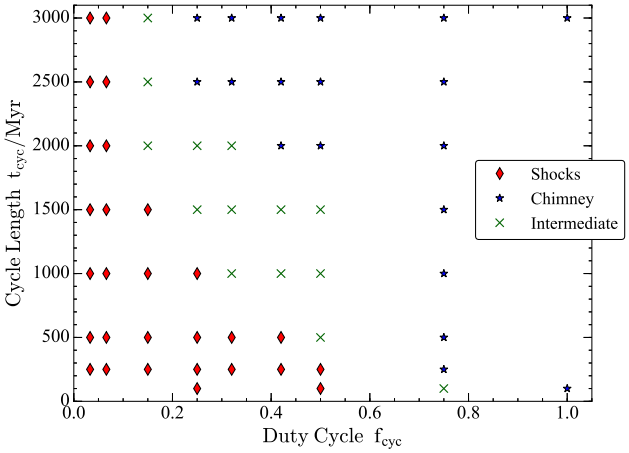

Figure 4. Distribution of shock-dominated and chimney-dominated outflow type with the variations of duty cycle and cycle length parameters. We make this classification by visual inspection of the outflows as described in the text. Red diamonds, blue stars and green crosses indicate the shock-dominated, chimney-dominated and intermediate cases. We have used the simulations with cooling enabled, but found that the differences in the case without cooling were minor. To maintain the average mass-loading, the density of the bubble scales in inverse proportion to the duty cycle, ranging from 1.7×10^4 $M_\odot$ kpc^{-3} for $f_{cyc} = 0.033$ to 6.1×10^2 $M_\odot$ kpc^{-3} for $f_{cyc} = 1.0$.

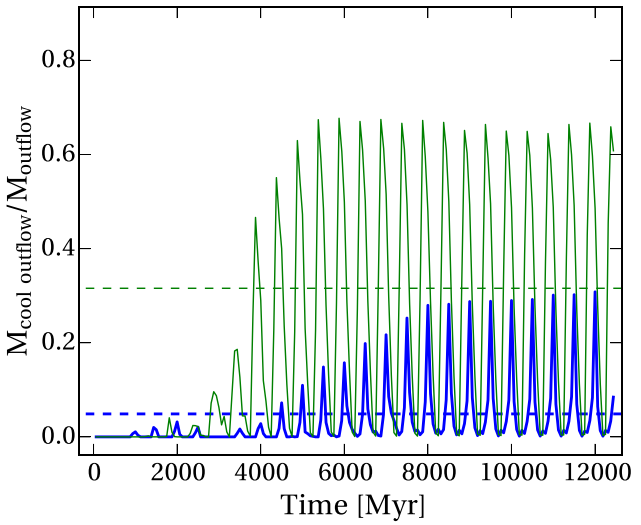

Figure 5. Cool gas fraction comparison between the galaxies illustrated in Fig. 3. For each timestep, the cool gas fraction is calculated as a mass fraction of outflowing gas ($v_y > 20$ km s^{-1}) that has temperatures satisfying $T < 5 \times 10^4$ K. The thinner, green line shows the case $f_{cyc} = 0.033$, whereas the thicker blue line shows the case $f_{cyc} = 0.75$. The time-averaged value for the two cases is shown by corresponding dashed horizontal lines and is 32 per cent and 5 per cent for the two respective cases.

the gas establishes a direct route out of the halo and so maintains its high initial outflow speed once the initial resistance of the cooling inflow has been cleared away. This high-speed, high-temperature, relatively low-density flow rarely reaches a regime where it cools efficiently.

To make a more quantitative comparison between the cases and their ability to generate cool outflows, we quantified the fraction of the outflowing mass that is cool in each case. We defined outflowing gas as having an upwards vertical velocity >20 km s^{-1} and 'cool' gas to be at temperatures $T < 5 \times 10^4$ K. For each snapshot, we then measured the cool outflow fraction by mass. The results for the two simulations that we have discussed so far are shown in Fig. 5; the thicker and thinner lines, respectively, are generated from the chimney-dominated $f_{cyc} = 0.75$ and shock-dominated $f_{cyc} = 0.033$ cases.

Over the first few cycles, the amount of cold gas forming in both cases grows. Eventually, a repeating cycle is established. Each cycle starts when the galaxy (below the box) starts injecting gas; at this point, the amount of cool gas becomes small as the injected material is hot and compresses any cold material. Once the outflow shuts off, the fraction of cool gas tends to grow as the shock expands outwards and radiative effects become significant behind the shock front. Short f_{cyc} values switch off the heating source earlier in the cycle and thus allow larger cool mass fractions to build up before the next cycle begins. This is reflected in the average, taken over the penultimate two cycles, of the cool mass fraction which is 32 per cent and 5 per cent in the $f_{cyc} = 0.033$ and 0.75 cases. These averages are shown by the horizontal dashed lines.

In Fig. 6, we show this average cool-mass fraction of outflows calculated for each simulation. The position on the plot shows the duty cycle and cycle length, and the size of the plotted dot is in proportion to the cool-mass fraction. The average is taken over gas outflowing at speeds greater than 50 km s^{-2} after 9 Gyr, when the cycle has become stable. Our summary statistic of the total cool mass fraction gives a sense of how observable the cool phase is likely to be, but we emphasize that the cool gas often occupies a

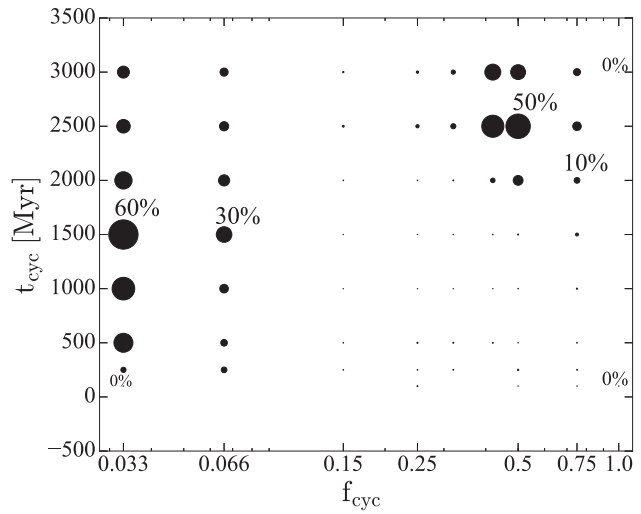

Figure 6. Duty cycle f_{cyc} distribution with the cycle length, t_{cyc} as shown in Fig. 4, but now the size of the circles show the amount of cool gas in the outflow and the percentages show the numeric value for a selection of models. Our results highlight two regimes in which cool gas is easiest to form; either a small duty fraction is required, giving relatively high outflow densities and so allowing gas to cool in between bursts, or the total cycle time must be long, yielding long time periods during which denser regions of the turbulent halo can cool.

relatively small volume and is only present in large quantities during certain parts of the cycle.

Outflows with our smallest duty cycle (i.e. on the left edge of the figure) are able to generate cool mass almost irrespective of the cycle length, although for $t_{cyc} \leq 100$ Myr, we find that the individual shocks occur so regularly that they prevent the gas from cooling. For long cycle lengths, $t_{cyc} \geq 2000$ Myr, we also find a slight decline in our cool mass fraction which is caused by the cool outflows being

slower in this regime (so that a smaller proportion pass the velocity cut).

We can also generate large cool-gas fractions in a few cases that we classified as chimneys (middle-top part of Fig. 6) at $f_{\rm cyc} = 0.5$, with $t_{\rm cyc} = 3000$ or 2500. In these cases, galaxies spend half their time injecting hot gas into the halo. This means that the halo is left undisturbed for a period of time >1 Gyr which is long enough for even relatively diffuse gas at $\sim 10^4\,{\rm M}_\odot\,{\rm kpc}^{-3}$ to cool. As seen in Fig. 3, there is gas at this density in the regions around our chimneys. However, for the cases where the cycle fraction reaches $f_{\rm cyc} = 0.75$ (towards the top right of the figure), the period for which the halo is undisturbed by incoming material becomes less than the cooling time of approximately 1 Gyr, and the cool gas fraction declines.

By contrast in the low-$f_{\rm cyc}$ regime, the regular shock fronts between new gas and the existing halo always reach high densities ($\gg 10^4\,{\rm M}_\odot\,{\rm kpc}^{-3}$), bringing the cooling time down to a few hundred Myr (depending on the exact temperature and density) and so allowing efficient cold gas formation.

Fig. 6 highlights the existence of a transition between $f_{\rm cyc} = 0.15$ and 0.25 which falls in between these cases and is unable to efficiently produce cool gas. In these cases, gas behind the shock is hotter and denser than its environment. In fact, we find that, during the 'off', relatively undisturbed phase, a portion of the halo does cool; however, it is slow-moving and starts to infall; it is therefore not counted since we made a cut to include only gas particles travelling faster than 50 km s^{-1}. The gas that is outflowing in these cases remains hot (10^5 K) and with low density ($\sim 80\,{\rm M}_\odot\,{\rm kpc}^{-3}$).

4 CONCLUSIONS

In this paper, we have considered the possibility that the cool gas material observed in outflows in the CGM is a consequence of *in situ* cooling (Thompson et al. 2016), using the RAMSES code. We do not simulate the disc in our galaxies; instead, we manually inject gas moving into the base of a box representing the halo (see also Mac Low & Ferrara 1999). We started by finding and testing equilibrium inflows to be sure that the effects we observe are a result of outflows rather than the choice of initial conditions; see equations (7)–(9). We used a fixed potential corresponding to a 50 km s^{-1} virial velocity dwarf galaxy. The cooling function $\dot{Q}_{\rm cool}$ we adopt is suitable for primordial gas as implemented by RAMSES, which underestimates the true cooling rates and so leads us to conservative conclusions.

We modified RAMSES to inject a time-varying flow into the bottom of the computational domain, according to a set of parameters summarized in Table 1. Our particular focus was on the role that varying star formation rates in the galaxy could have on the evolution of outflows as they traverse the halo. From the complete set of parameters characterizing outflows, we therefore varied two: the overall star formation cycle length, $t_{\rm cyc}$, and the fraction of that time spent pumping gas into the CGM, $f_{\rm cyc}$. We varied these while keeping the total energy injection and mass-loading constant. We found a close connection between the parameters and the overall nature of the outflows' traversal of the CGM (Fig. 4). This, in turn, has a strong effect on the multiphase nature of the outflows.

The amount of cooler $T < 5 \times 10^4$ K gas present in the outflow varies strongly over the course of a cycle (Fig. 5). Cool material is typically able to form as a shock propagates outwards provided that no hot material is being injected behind the shock. This leads to the time-averaged cool mass fraction depending on both $t_{\rm cyc}$ and $f_{\rm cyc}$ (Fig. 6). There are two regimes in which we obtain large cool mass fractions: the first has a small $f_{\rm cyc}$, corresponding to a rapidly fluctuating star formation rate. Provided $t_{\rm cyc}$ is greater than a few hundred Myr, the successive shocks do not join up into a coherent flow and the strong time variability triggers waves of effective cooling that travel through the CGM. The second approach is to leave a long period $\gtrsim$1 Gyr between successive star formation epochs; in this case, cool gas is able to form in the turbulent halo left behind when ejection from the disc shuts off. Our results suggest that steady flow or single-burst solutions with cooling (Thompson et al. 2016) form a lower bound on the amount of *in situ* cooling to be expected in realistic galaxies with time-varying feedback.

Our interest in cool gas is motivated by observational results that show the presence of a cool phase even at large distances from Galactic Centres (e.g. Nielsen et al. 2013), which is hard to explain in entrainment scenarios (Zhang et al. 2015). However, it would be premature to compare our highly idealized study directly to observations. To enable our large parameter study, we had to restrict ourselves to two-dimensional solutions; the detailed behaviour in three dimensions could differ significantly. Other neglected aspects of the problem include the enhanced cooling rates from metal enrichment and the effects of thermal conduction and magnetic fields. Furthermore, a realistic cosmological environment is far more complex than the uniform inflow solution that forms our initial conditions. In terms of the cooling rates, neglecting metals leads to a conservative bound; i.e. more realistic simulations may be able to form cold clouds more easily than our work suggests.

We hope to use our results to interpret the CGM around ab initio cosmological galaxy formation simulations. Some feedback algorithms enforce relatively steady-state star formation (e.g. Dalla Vecchia & Schaye 2008; Oppenheimer & Davé 2008; Vogelsberger et al. 2014; Schaye et al. 2015) whereas others lead to strong bursts (e.g. Hopkins et al. 2014; Keller, Wadsley & Couchman 2015) and the importance of this distinction for galactic dynamics has already been established (Pontzen & Governato 2014). In future work, we will study what role *in situ* cooling plays in these different scenarios, and make the link to observational constraints on the rich phenomenology of the CGM.

ACKNOWLEDGEMENTS

We thank the referee, Evan Scannapieco, for a helpful report with many useful suggestions. TS acknowledges support via studentships from CONACyT (Mexico) and the University College London. AP is supported by the Royal Society. HVP was supported by the European Research Council under the European Community's Seventh Framework Programme (FP7/2007- 2013)/ERC grant agreement no 306478-CosmicDawn. The simulations were analysed using PYNBODY (Pontzen et al. 2013). This work used the DiRAC Complexity system, operated by the University of Leicester IT Services, which forms part of the STFC DiRAC HPC Facility (www.dirac.ac.uk). This equipment is funded by BIS National E-Infrastructure capital grant ST/K000373/1 and STFC DiRAC Operations grant ST/K0003259/1. DiRAC is part of the National E-Infrastructure.

REFERENCES

Ajiki M. et al., 2002, ApJ, 576, L25
Bordoloi R. et al., 2014, ApJ, 796, 136
Bustard C., Zweibel E. G., D'Onghia E., 2016, ApJ, 819, 29
Christensen C. R., Davé R., Governato F., Pontzen A., Brooks A., Munshi F., Quinn T., Wadsley J., 2016, ApJ, 824, 57
Dalla Vecchia C., Schaye J., 2008, MNRAS, 387, 1431
Dekel A., Silk J., 1986, ApJ, 303, 39

Efstathiou G., 2000, MNRAS, 317, 697
Erb D. K., 2015, Nature, 523, 169
Finlator K., Davé R., 2008, MNRAS, 385, 2181
Governato F. et al., 2010, Nature, 463, 203
Haardt F., Madau P., 2012, ApJ, 746, 125
Hopkins P. F., Quataert E., Murray N., 2012, MNRAS, 421, 3522
Hopkins P. F., Kereš D., Oñorbe J., Faucher-Giguère C.-A., Quataert E., Murray N., Bullock J. S., 2014, MNRAS, 445, 581
Keller B. W., Wadsley J., Couchman H. M. P., 2015, MNRAS, 453, 3499
Le Bret T., Pontzen A., Cooper A. P., Frenk C., Zolotov A., Brooks A. M., Governato F., Parry O. H., 2015, preprint (arXiv:1502.06371)
Mac Low M.-M., Ferrara A., 1999, ApJ, 513, 142, ApJ, 513, 142
Macciò A. V., Dutton A. A., van den Bosch F. C., Moore B., Potter D., Stadel J., 2007, MNRAS, 378, 55
Martin C. L., 1999, ApJ, 513, 156
Martin C. L., 2005, ApJ, 621, 227
Martin C. L., Dijkstra M., Henry A., Soto K. T., Danforth C. W., Wong J., 2015, ApJ, 803, 6
Murray N., Quataert E., Thompson T. A., 2005, ApJ, 618, 569
Nesvadba N. P. H., Lehnert M. D., De Breuck C., Gilbert A. M., van Breugel W., 2008, A&A, 491, 407
Nielsen N. M., Churchill C. W., Kacprzak G. G., 2013, ApJ, 776, 115
Oñorbe J., Boylan-Kolchin M., Bullock J. S., Hopkins P. F., Kereš D., Faucher-Giguère C.-A., Quataert E., Murray N., 2015, MNRAS, 454, 2092
Oppenheimer B. D., Davé R., 2008, MNRAS, 387, 577
Oppenheimer B. D., Davé R., Kereš D., Fardal M., Katz N., Kollmeier J. A., Weinberg D. H., 2010, MNRAS, 406, 2325
Peeples M. S., Werk J. K., Tumlinson J., Oppenheimer B. D., Prochaska J. X., Katz N., Weinberg D. H., 2014, ApJ, 786, 54
Pontzen A., Governato F., 2012, MNRAS, 421, 3464
Pontzen A., Governato F., 2014, Nature, 506, 171
Pontzen A., Roškar R., Stinson G., Woods R., 2013, Astrophysics Source Code Library
Pontzen A., Read J. I., Teyssier R., Governato F., Gualandris A., Roth N., Devriendt J., 2015, MNRAS, 451, 1366
Rees M. J., Ostriker J. P., 1977, MNRAS, 179, 541
Rubin K. H. R., Weiner B. J., Koo D. C., Martin C. L., Prochaska J. X., Coil A. L., Newman J. A., 2010, ApJ, 719, 1503
Scannapieco E., Brüggen M., 2015, ApJ, 805, 158
Schaye J. et al., 2015, MNRAS, 446, 521
Strickland D. K., Heckman T. M., Colbert E. J. M., Hoopes C. G., Weaver K. A., 2004, ApJ, 606, 829
Teyssier R., 2002, A&A, 385, 337
Thompson T. A., Quataert E., Zhang D., Weinberg D. H., 2016, MNRAS, 455, 1830
Veilleux S., Cecil G., Bland-Hawthorn J., 2005, ARA&A, 43, 769
Vogelsberger M. et al., 2014, MNRAS, 444, 1518
Werk J. K. et al., 2014, ApJ, 792, 8
Zhang D., Thompson T. A., Quataert E., Murray N., 2015, preprint (arXiv:1507.01951)

This paper has been typeset from a TEX/LATEX file prepared by the author.